

RSC Advances



This is an *Accepted Manuscript*, which has been through the Royal Society of Chemistry peer review process and has been accepted for publication.

Accepted Manuscripts are published online shortly after acceptance, before technical editing, formatting and proof reading. Using this free service, authors can make their results available to the community, in citable form, before we publish the edited article. This *Accepted Manuscript* will be replaced by the edited, formatted and paginated article as soon as this is available.

You can find more information about *Accepted Manuscripts* in the [Information for Authors](#).

Please note that technical editing may introduce minor changes to the text and/or graphics, which may alter content. The journal's standard [Terms & Conditions](#) and the [Ethical guidelines](#) still apply. In no event shall the Royal Society of Chemistry be held responsible for any errors or omissions in this *Accepted Manuscript* or any consequences arising from the use of any information it contains.

Cite this: DOI: 10.1039/c0xx00000x

www.rsc.org/xxxxxx

ARTICLE TYPE

Ni/Mn ratio and morphology-dependent crystallographic facet Structure and electrochemical properties of high-voltage spinel $\text{LiNi}_{0.5}\text{Mn}_{1.5}\text{O}_4$ cathode material

Lina Wan^a, Yuanfu Deng^{*a,b}, Chunxiang Yang^a, Hui Xu^b, Xusong Qin^b and Guohua Chen^{*b,c}

5 Received (in XXX, XXX) Xth XXXXXXXXX 200X, Accepted Xth XXXXXXXXX 200X

DOI: 10.1039/b000000x

The $\text{LiNi}_{0.5}\text{Mn}_{1.5}\text{O}_4$ (LNMO) spinel is an attractive cathode material for next generation lithium-ion batteries as it offers high power capability with a discharge voltage of 4.7 V and a theoretical capacity of 147 mAh g^{-1} . In this paper, porous LNMO microspheres/cubes, which are constructed with nanometer-
10 sized primary particles with different Ni/Mn ratio, have been synthesized by a facile method that involves the use of MnCO_3 microspheres/cubes as the self-supporting template. The effects of the morphology of the MnCO_3 and the Ni/Mn ratio on the physicochemical and electrochemical properties of the as-synthesized LNMO materials were investigated in detail. Scanning electron microscope (SEM)
15 observation shows that the morphology of the porous MnCO_3 has important effect on the morphology and degree of dispersion of the obtained LNMO spinels, so as to the electrochemical performance. XPS and XRD results show that the Ni/Mn ratio has significant impacts on the Mn^{3+} content, phase purity (rock-salt phase) and crystallographic facet orientations of the LNMO-based cathode materials. In particular, the Mn^{3+} content, rock-salt phase and high-active (111) facet in the LNMO spinels were found to be adjusted by the Ni/Mn ratio. With the presence of reasonable Mn^{3+} content, high-active facet, the absence
20 of the impurity phase (rock-salt phase) as well the large cationic disorder in the Cr-doping LNMO spinels, the rate performance and capacity retention of the product could be significantly improved. All these findings show the important roles of the synergic effects of the morphology and the composition on the improvement electrochemical performance of LNMO-based cathode materials.

Introduction

25 Lithium ion batteries (LIBs) are expected to make a great impact on pure electric vehicles (EVs) and plug-in hybrid electric vehicles (PHEVs) in the near future.^{1,2} Developing electrode materials with high energy and power densities, long cycle life, low cost and high safety is one of the key challenges for adopting
30 the lithium-ion battery technology for the EVs and the HEVs applications.³ For instance, the spinel cathode LiMn_2O_4 has been commercialized in the first generation of PHEVs and EVs, but has met with mixed success.⁴ However, the durability of such a material and to a less extent their limited rate capability are still a
35 lasting issue. In order to satisfy the demands of the public and achieve a broader adoption, the energy and power capability must be increased. Thus, novel cathode materials with high energy and power densities have received considerable interest.⁴

40 With a high operating voltage around 4.7 V and a practical capacity (about 130 mAh g^{-1}) comparable to that of LiCoO_2 (~140 mAh g^{-1}) and LiFePO_4 (~160 mAh g^{-1}), spinel $\text{LiNi}_{0.5}\text{Mn}_{1.5}\text{O}_4$ (LNMO) provides a specific energy (~610 Wh kg^{-1}) higher than that of many commercialized compounds.⁵ The attractive feature, along with rapid Li^+ ion transport via three-
45 dimensional diffusion channels in the lattice⁶ and the relatively

benign constituent elements, have made this material a good choice for the next generation of high-power batteries.⁴ However, the electrochemical performance of this high-voltage spinel cathode material is influenced by a variety of factors that depend
50 on how it is synthesized and processed. The main factors include the cationic doping/ordering,⁷⁻²² morphology²³⁻²⁸ and crystal surface planes^{26,27,29-31} of the prepared LNMO-based cathode materials.

There are four main problems result in the capacity fade for
55 LNMO material. The first one is the formation of a solid-electrolyte interphase (SEI) layer through undesired side reactions with the electrolyte under the high operating voltage.⁴ In addition, cationic ordering between the Mn^{4+} and Ni^{2+} ions in the crystal lattice is thought to decrease the electronic
60 conductivity and has been shown to cause a large lattice parameter difference among the three cubic phases which formed during charge-discharge reactions.^{13,17,32} Capacity fade has also been attributed to the formation of a rock salt $\text{Li}_x\text{Ni}_{1-x}\text{O}$ impurity phase during high-temperature synthesis, which introduces Mn^{3+}
65 ions into the structure.^{6,13} The impact of Mn^{3+} defects has been thoroughly examined, but the results are controversial. Some believe that the existence of Mn^{3+} is helpful to stabilize the cycling performance and to improve the stability.^{18,21,30,33,34} The

Mn³⁺ induces more Ni and Mn disordering with a higher proportion of *Fd-3m* lattice, thus improves Li ion transport coefficient and the electrical conductivity of LNMO. Others argue that Mn³⁺ ions have higher tendency to disproportionate by $2\text{Mn}^{3+} \rightarrow \text{Mn}^{2+} + \text{Mn}^{4+}$.³⁵ The Mn²⁺ ion can easily dissolve in electrolyte and is capable to electrochemically deposit at anode surface after passing through membrane, resulting in adverse influence for the cycling performance.^{36,37} An emerging finding is that the particle morphology (include the surface crystallographic planes) influences the electrochemical properties, especially the rate performance of the LNMO material.²³⁻³⁰ Many efforts have been made to optimize the performance of this LNMO spinel material and a great of advance has been achieved in recent years.^{4,5,38} However, the role of synthesis methods and conditions in the above parameters and electrochemical performance has not been fully established. Also, no papers have been reported on the effect of the surface crystallographic planes on the long cycle performance at high charge and discharge current density, as far as we know.

More recently, attention turned to preparation of the LNMO-based cathode materials with nanometer particle to enhance their cyclic performance, and especially the rate performance.^{28,31,39-43} Generally, the smaller the particles size is, the shorter the lithium ion diffusion distance and the electron transfer distance are, the better the rate capability is.³³ The use of nanomaterials in electrode fabrication, on the other hand, has some disadvantages, such as high viscosity of slurry, low tap density, both of which result in low active materials coated and thus low volumetric energy density.⁴⁴ These shortcomings of nano-scaled LNMO materials and their complicated synthesis routes hinder their industrial application on large scale, such as for PHEVs or EVs. To achieve both excellent rate capability and high volumetric energy density, it is desired that the micrometer particles composed of aggregated nano-sized particles can form three-dimensional channels for ion diffusion.⁴⁵⁻⁴⁷ In electrode processing, this kind of particles also leads to high loading and is able to better accommodate the volume change and to reduce the electrode tension upon cycling.

In this paper, we report a facile solid state method of preparing micrometer-sized porous LNMO spheres/cubes, which were constructed with nanometer-sized primary particles, aiming to obtain LNMO-based cathode materials with high specific capacity, high rate and durable cycle performance. The formation of porous LNMO cathode materials were achieved by using porous MnCO₃ with different morphologies as the self-supporting template, into which eutectic molten lithium salt was inserted for reaction.⁴⁸ The effect of the morphologies of the porous MnCO₃ precursors as well the Ni/Mn ratio on the morphologies, phase structure, cationic disorder, crystallographic facet orientations, the Mn³⁺ content in the surface and the electrochemical performance of the as-prepared LNMO cathode materials have been investigated systematically and to choose the best LNMO cathode material with reasonable chemical composition and morphology.

Experimental

Synthesis of spherical MnCO₃

In a typical synthesis, two stock solution of MnSO₄ (0.01 mol

MnSO₄·H₂O in 420 mL distilled water) and NaHCO₃ (0.04 mol NaHCO₃ in 420 mL deionized water) were first prepared. Then, the NaHCO₃ solution were added into the MnSO₄·H₂O solution slowly under stirring. The mixture was maintained at room temperature for 3 h under stirring constantly. Finally, the white powder was filtered, washed by deionized water and ethanol three times and dried in vacuum at 60 °C overnight to obtain ~3.0 μm microspheres.

Synthesis of cubic MnCO₃

The cubic MnCO₃ was obtained by the previous reported method with some modification.⁴⁹ In a typical experiment, Nanoseed solution was prepared firstly (4 mg NH₄HCO₃ and 0.1 mg MnSO₄ dissolved in 20 mL distilled water). Then, 6 mmol MnSO₄ was dissolved in 1 L of deionized water with 5 mL 2-Propanol (IPA), and this solution was mixed with 1 L of 0.06 mol/L NH₄HCO₃ with 5 mL IPA and 9 mL of the as-prepared nanoseed solution. This mixed solution was stirred at ~200 rpm for 2 h at 50 °C. Finally, the white powders were filtered, washed by deionized water and ethanol three times and dried in vacuum at 60 °C overnight to obtain ~3.0 μm microcubes.

Synthesis of LNMO-based spinel cathode materials

The LiNi_{0.5-x}Mn_{1.5+x}O₄ ($x = 0$ and ± 0.05) cathode materials with different morphologies were prepared by a solid state reaction using the MnCO₃ as self-template. In a typical procedure, firstly, stoichiometric proportions of ~3.0 μm MnCO₃ microspheres, Ni(NO₃)₂·6H₂O and the eutectic molten lithium salt of LiOH·H₂O and Li₂CO₃ (0.38:0.62 in mol ratio) were dispersed in ethanol under continuous stirring, the mixture was evaporated at 55 °C and ground manually for several minutes, then the obtained powder was sintered in air at 430 °C for 3 h and then at 800 °C for 20 h. Finally, the calcination product was cooled down to room temperature naturally to achieve the final sample. Specifically, sample of S-1.50, was used to represent the product obtained from the spherical MnCO₃ precursors with 3.0 μm and Ni/Mn ratio of 0.5:1.50. Other LNMO-based samples were prepared by spherical MnCO₃ precursor and manganese theoretical excess of -0.05 and 0.05 were tagged as S-1.45 and S-1.55, respectively. Other LNMO-based samples were prepared by cubic MnCO₃ precursor and manganese theoretical excess of 0 and 0.05 were tagged as C-1.50 and C-1.55, respectively.

The LiNi_{0.45}Mn_{1.5}Cr_{0.05}O₄ (C-Cr) was prepared by the similar procedures for the preparation of C-1.55 sample except that additional Cr(NO₃)₃·6H₂O was added into the precursors.

Physical characterizations

The structures and morphologies of the as-prepared materials were characterized by powder X-ray diffraction (XRD, Bruker D8 ADVANCE powder diffractometer using Cu Kα radiation at 40 kV and 40 mA at steps of 0.020), field emission scanning electron microscopy (SEM, JEOL 6300F scanning electron microscope), transmission electron microscopy (TEM, Philips Tecnai-F20, 200 kV) and high-resolution TEM (HRTEM). X-ray photoelectron spectroscopy (XPS) measurements were performed with a Kratos Axis Ultra spectrometer using a focused monochromatized Al Kα radiation ($h\nu = 1486.6$ eV). The binding energy was calibrated with reference to the C_{1s} level of carbon (285.0 eV). Raman spectra were obtained with a Bio-Rad FTS6000 Raman microscopy with a 532 nm blue laser beam. Fourier transform infrared (FT-IR) spectra were recorded with

KBr pellets on a Bruker R 200-L spectrophotometer. The compositions of the selective samples were tested by inductively coupled plasma (ICP) analysis on Optima 7300DV analyzer (PerkinElmer).

5 Electrochemical studies

Electrochemical performances of the LNMO cathode materials were evaluated with CR2025 coin half-cells. The composite electrodes consisted of 80 wt% LNMO, 10 wt% acetylene black and 10wt% polyvinylidene fluoride (PVDF) by weight and were prepared by coating the mixture on aluminum foils with typical active material loading of $\sim 2.5 \text{ mg cm}^{-2}$. The 2025 coin cells in the test used lithium foil as the counter electrode, polypropylene micro porous membrane as the separator and 1M LiPF_6 dissolved in ethylene carbonate (EC) and ethyl methyl carbonate (EMC) (3:7, v/v) as the electrolyte. The cells were assembled in an argon-filled glove box. The assembled cells were cycled between 3.2 and 4.9 V at different rates using a Neware Battery Testing System (CT3008W). The specific capacity calculated based on mass of active material. The cyclic voltammetric (CV) tests were carried out on an Electrochemical Workstation (Autolab PGSTAT 101) at different scan rates in the range of 3.5–4.9 V vs. Li/Li^+ . The electrochemical impedance spectroscopy (EIS) data of the electrodes were acquired at the room temperature by a Versa-stat 3 electrochemical workstation (Princeton Applied Research) before cycling and also after a desired number of cycles, respectively, at a constant potential of approximately 4.7 V (vs Li/Li^+) in the frequency range from 100 kHz to 10 mHz by imposing an alternate current with an amplitude of 10 mV on the electrodes

30 Results and discussion

The morphologies of the synthesized MnCO_3 are presented in Figure S1. As shown in Figure S1a, the as-prepared MnCO_3 by the reactions of $\text{MnSO}_4 \cdot \text{H}_2\text{O}$ and NaHCO_3 in aqueous solution adopts spherical shape with average size of $\sim 3 \mu\text{m}$. When mixing $\text{MnSO}_4 \cdot \text{H}_2\text{O}$ and NH_4HCO_3 solutions in the presence of the previously prepared nanoseed,⁴⁹ MnCO_3 in the cubic shape (Figure S1b) was obtained. It has been shown that the reaction conditions have a strong effect on the nucleation and growth of manganese carbonate precursors in aqueous solution, which in turn has a significant effect on the electrochemical performance of the final spinel LNMO^{25,31,45} and LiMn_2O_4 ⁴⁸ cathode materials. Because of the eutectic molten lithium salt has a higher ion diffusion rate and strong dissolving capability,^{25,50} the MnCO_3 self-template with link of molten-salt route has an accelerated reaction rate and controllable sample morphologies. When using the obtained spherical MnCO_3 with $\sim 3 \mu\text{m}$ as self-templates and precursors, the LNMO cathode materials with porous spherical shape in $\sim 3 \mu\text{m}$ (Figure S2a to S2c) were achieved. If the cubic MnCO_3 as precursor, the LNMO-based samples with cubic structure in $\sim 3 \mu\text{m}$ (Figure S3a to S3c) were obtained. In order to check the microstructure of LNMO samples with different morphologies, Figure 1 shows the high resolution SEM images of the S-1.55 and C-1.55 samples. Both of samples were composed of many nanometer-sized primary particles. However, the primary particles morphology of the two samples are some

difference and the particle size of C-1.55 are bigger than those of S-1.55. This different morphology of the two samples may result the different crystal orientation, which is demonstrated by the following XRD patterns.

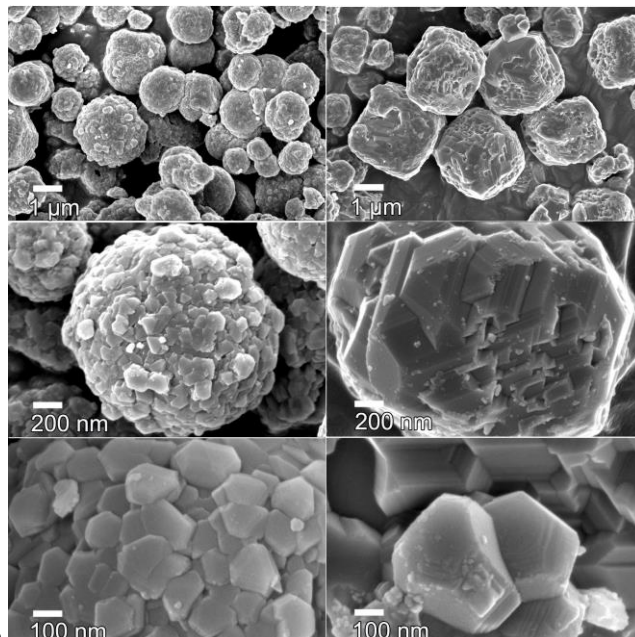


Figure 1. High resolution SEM images of the S-1.55 (a-c) and C-1.55 (d-f) samples.

The chemical compositions of the obtained six LNMO-based samples are measured by ICP/AES method, and the obtained results are listed in Table 1. For each x value, the Ni/Mn ratio in the obtained samples is approximately the same as that of the corresponding raw materials. This means that the synthetic method for preparation of the LNMO-based spinels is reliable.

Table 1. Composition analysis data of the selective six various LNMO samples by the ICP data.

sample	Ni [mol]	Mn [mol]	Li [mol]	Cr [mol]
S-1.45	0.552	1.45	0.99	0
S-1.50	0.503	1.50	1.01	0
S-1.55	0.453	1.55	1.00	0
C-1.50	0.505	1.50	0.99	0
C-1.55	0.452	1.55	1.00	0
C-Cr	0.453	1.50	1.00	0.049

Figure 2 shows the XRD patterns of the obtained six LNMO-based cathode materials. All of the samples display good crystallinity and all of the diffraction peaks can be indexed to cubic spinel structure with $Fd-3m$ space group. In addition, the $\text{LiNi}_{0.5}\text{Mn}_{1.5}\text{O}_4$ (S-1.50 and C-1.50) and $\text{LiNi}_{0.55}\text{Mn}_{1.45}\text{O}_4$ (S-1.45 samples) show some weak peaks at $2\theta = 37.6^\circ$, 43.7° , and 63.5° , which could be attributed to the cation-rich rock salt phase impurities ($\text{Li}_y\text{Ni}_{1-y}\text{O}$, ICSD No. 71422). It is worth noting that there is no obvious impurity phase observed for the $\text{LiNi}_{0.45}\text{Mn}_{1.55}\text{O}_4$ (S-1.55 and C-1.55) and $\text{LiNi}_{0.45}\text{Mn}_{1.50}\text{Cr}_{0.05}\text{O}_4$ samples. This is an interesting observation as it suggests that the Ni/Mn ratio and Cr-substitution employed here can simply adjust the phase purity for LNMO-based spinels. The lattice parameters (a value/Å) for S-1.45, S-1.50 and S-1.55 were calculated (by

the Jade 5.0 software) to be 8.1805, 8.1795 and 8.1830(± 5), respectively. The highest lattice parameters of S-1.55 may be attributed to the highest Mn^{3+} content in this sample. Because the ionic radius of Mn^{3+} (0.645 Å) is larger than that of Mn^{4+} (0.53 Å). This result is consistent with the fact of the largest diffraction 2 θ angle of (111) peak for S-1.50 spinel (as shown in Figure 2, inserted). Similarly, the lattice parameter of C-1.55 (8.1825(± 5) Å) is larger than that of and C-1.50 (8.1803(± 5) Å). After 5% of the Ni is substituted with Cr, the lattice parameter 8.1805 (± 5) Å is almost the same as C-1.5 (8.1803 Å), which is much smaller than that of C-1.55 sample (8.1825 Å). Previous study result showed that substitution of 5% Ni by Cr induced more Mn^{4+} to be reduced to Mn^{3+} due to charge neutrality and increased the lattice parameter.¹⁸ However, our XRD results show that the lattice parameters of the C-1.5 and C-Cr are very close, which may be caused by the oxygen nonstoichiometry in C-1.5 sample, resulting in more high Mn^{3+} content in this sample. These results suggest that the experiment condition employed in this work, that is, the MnCO_3 precursors with different morphologies, the different Ni/Mn ratio and Cr-substitution have important effect on the Mn^{3+} content in the LNMO-base spinels. These Mn^{3+} content adjustments have important role on the electrochemical performance of the spinel LNMO as a cathode material for LIBs as seen subsequently.

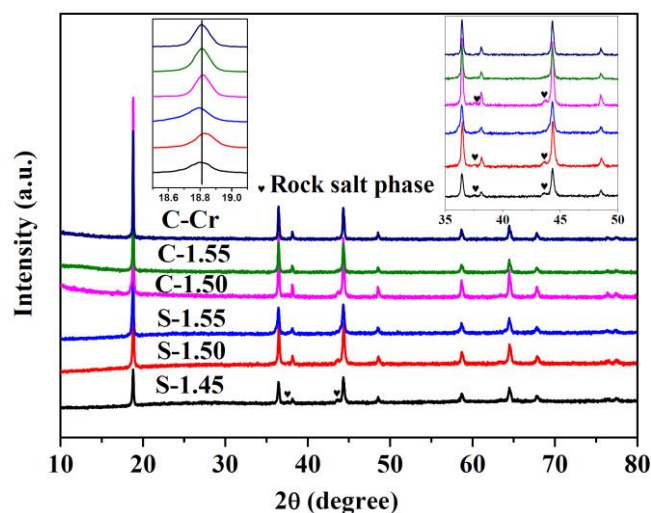


Figure 2. The XRD patterns of the as-synthesized LNMO-based materials.

It is reported that the relative peak intensities reflect the relative exposure degree of surface orientations in the spinel structure.^{31,51,52} A detail comparison of the XRD patterns among the six samples, which are normalized by the (311) peak, is presented in Figure 3. Comparing the three spherical LNMO samples with different Ni/Mn ratio, it is interesting to observe that the S-1.55 exhibits the strongest diffraction peak of (111) facet, which suggests that it possess the largest exposure of high-active crystal facet of (111) in the three samples.³¹ Between the S-1.55 and C-1.55 samples, when all of the peaks are normalized by the peak assigned to the (311) facet, the C-1.55 sample exhibits more intensified peak corresponding to the (111) facets. This observation suggests that the cubic LNMO shows stronger peak of (111) facet than the spherical LNMO with the same constitution.^{26,30,31} Among the three cubic samples (C-1.50, C-

1.55 and C-Cr), the relative (111) facet peak intensity is very close. Based on the above-mentioned results, it may suggest that the exposure of high-active crystal facets can be adjusted by the morphology, Ni/Mn ratio and substitution of Ni by Cr of the LNMO samples. It is also expected that the more high-active facets will be beneficial for achieving good rate capability and excellent cycle stability for the LNMO-based samples.

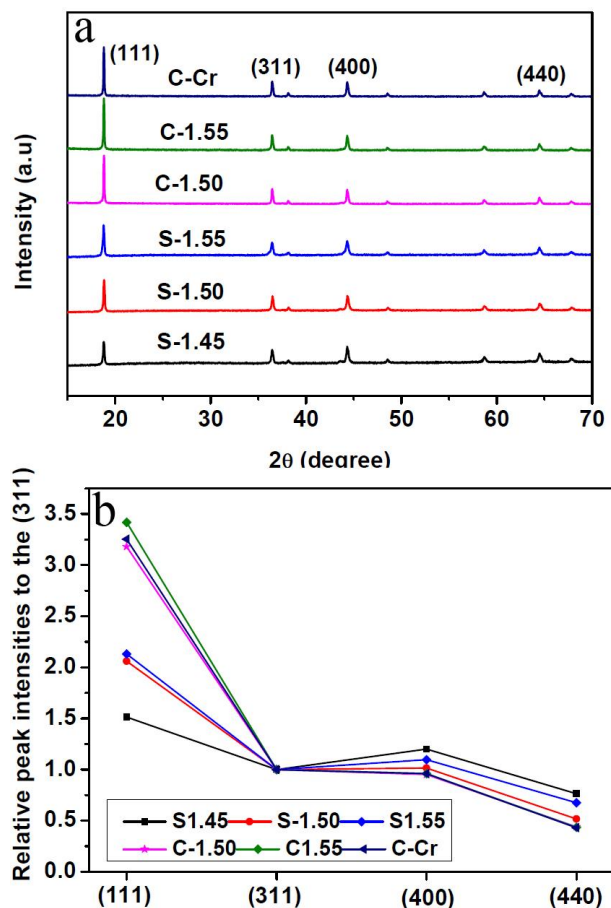


Figure 3. The XRD patterns of the as-synthesized LNMO-based materials normalized by the (311) peak.

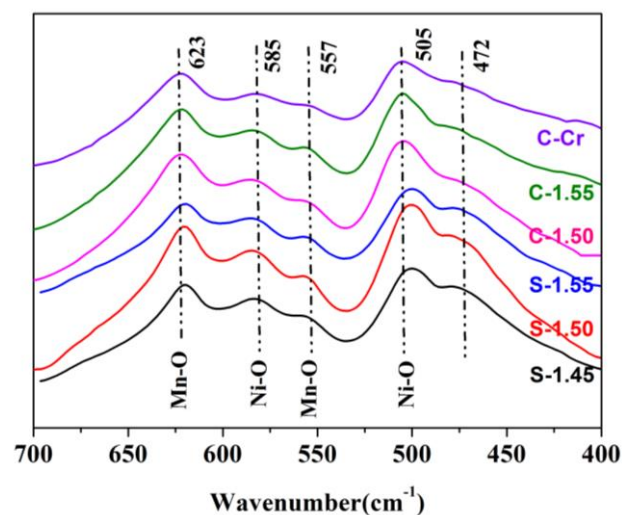


Figure 4. IR spectra of the as-synthesized LNMO samples.

To determine the degree of bulk cation ordering in the LNMO materials resulting from different precursors, FT-IR was employed. Infrared spectroscopy is a sensitive probe to the local structure of materials and has been demonstrated to be a useful tool to monitor the degree of Ni/Mn ordering in LNMO.^{6,53} Figure 4 shows the FT-IR absorbance spectra for a series of the obtained LNMO-based materials. The obtained six samples display similar FT-IR spectra, which are in accordance with that reported for disordered (*Fd-3m*) LNMO.⁵³ The spectra of the disordered samples consist of five broad and ill-defined bands that can be mainly attributed to vibrations associated with Mn–O and Ni–O bonds.

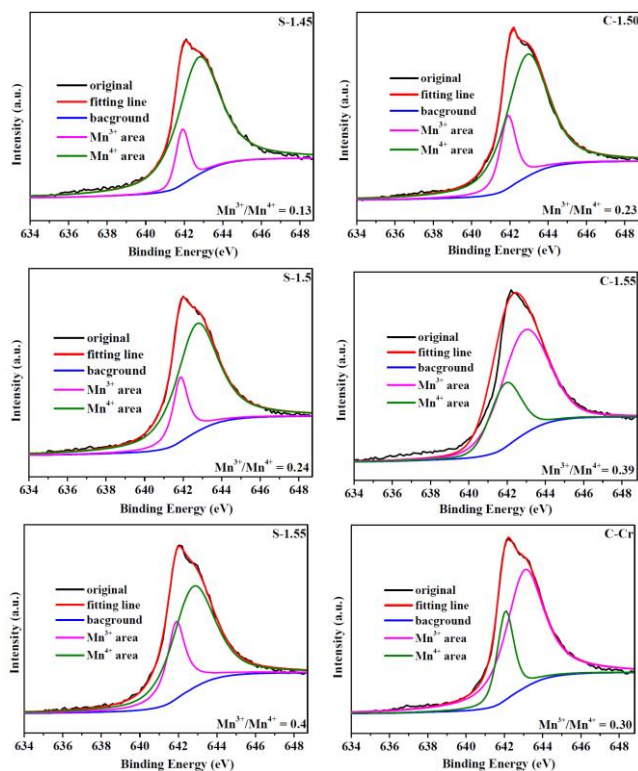


Figure 5. Fitting XPS of the Mn 2p_{3/2} peak of the as-synthesized LNMO samples.

To determine the surface oxidation state of Mn in the six LNMO-based spinels, the literature data for the binding energies of Mn³⁺ and Mn⁴⁺ are taken into account. It has been found that the binding energy for Mn⁴⁺ (642.7 eV) in MnO₂ is higher than that of Mn³⁺ (612.1 eV) in Mn₂O₃.⁵⁴ Figure S4 and Figure 5 respectively show the full XPS of Mn element and the detailed XPS fitting results of Mn³⁺ and Mn⁴⁺ on the surface of the six samples. The corresponding mole ratios of Mn³⁺/Mn⁴⁺ are listed in Table 2. Based on these fitting results, it is suggested that the Mn³⁺ content on the spinel surface is connected to the Mn/Ni mol ratio that used for the preparation of the LNMO-based materials. As shown in Table 2, the ratios of Mn³⁺/Mn⁴⁺ on the surfaces of all the samples are larger than those in their corresponding bulk materials (as calculated by the electrochemical discharge results voltage at ~ 4.0 V). This observation might be caused by the easy loss of oxygen on the surface of the spinels during the preparation process, making much more oxygen deficiency sites at the surface. For the spherical LNMO-based samples with different

composition, the ratio of Mn³⁺ to Mn⁴⁺ (Mn³⁺/Mn⁴⁺) increases with the decrease of the Ni/Mn ratio in the samples. This result is in good agreement with the XRD analysis predicted the enriched Mn³⁺ content in the S-1.55 sample. Among the S-1.55, C-1.55 and C-Cr samples, the Mn³⁺ content at the surface of the S-1.55 and C-1.55 is very close, but is much higher than that of the C-Cr sample. The above results demonstrate that the Ni/Mn ratio in the LNMO-based samples (not the morphology) mainly makes the Mn³⁺ content difference.

Table 2. Mn 2p_{3/2} peak positions and cation distribution in LNMO-based samples.

sample	binding energy position (eV)		cation distribution		
	Mn ⁴⁺	Mn ³⁺	Mn ⁴⁺ (%)	Mn ³⁺ (%)	Mn ³⁺ /Mn ⁴⁺
S-1.45	642.7	642.1	0.117	0.883	0.13
S-1.50	642.9	642.0	0.809	0.191	0.24
S-1.55	642.7	642.1	0.713	0.287	0.40
C-1.50	642.9	642.2	0.809	0.190	0.23
C-1.55	642.8	642.2	0.717	0.283	0.39
C-Cr	642.9	642.2	0.768	0.232	0.30

The electrochemical intercalation/deintercalation behaviors of the obtained six LNMO-based samples were examined through galvanostatic charge/discharge cycling using 2025 coin cells. The cells were charged at 0.5-C rate in the first two cycle without additional constant voltage modes and then charged at different current densities 0.5 to 10-C rate) with additional constant voltage modes. Figure 6a shows the first charge/discharge curves of the six samples at the charge/discharge current of 0.5-C rate (1 C = 147 mA g⁻¹), two separated charge plateaus, which were attributed to the Ni²⁺/Ni³⁺ and Ni³⁺/Ni⁴⁺, respectively, as well as a small plateau at ~ 4.0 V (Mn³⁺/Mn⁴⁺) can be clearly observed for the obtained LNMO-based electrode, which confirms that the LNMO-based samples crystallized in the cation-disorder phase.²² As shown in Figure 6b, the two-plateaus between 4.6 and 4.8 V are more pronounced and the gap between them is the largest in the six samples. This result confirms that the Cr-doping increases the cationic disorder.^{22,55} The S-1.45, S-1.50, S-1.55, C-1.50, C-1.55 and C-Cr shows a specific discharge capacity of 110.6, 118.5, 120.1, 118.7, 122.5, and 126.3 mAh g⁻¹ with a columbic efficiency (CE) of 71.6, 73.7, 72.9, 70.0, 76.5 and 82.0%, respectively. The low CE in the first cycle of the LNMO-based cathodes is attributed to the decomposition of the electrolyte at high voltage.¹⁸ The highest CE of the C-Cr sample suggests that the most stable electrode/electrolyte interface. In addition, the large differences in the specific discharge capacities of these samples are related to their different microstructures and compositions. Because of the absence of rock-salt phase in the Mn-riched and Cr-substituted samples, these three samples display high specific capacity. Meanwhile, the capacity from the ~ 4 V plateau in the Mn-riched samples (S-1.55 and C-1.55) are much higher than those in other four samples (S-1.45, S-1.5, C-1.5 and C-Cr). The length of the plateau in the 4 V region can be adopted to calculate the relative amount of residual Mn³⁺ content in the spinels. Detailed analysis was conducted to calculate the capacity percentage contribution from the Mn³⁺ plateau (4 V) for all the six samples, which are calculated from the discharge capacity of the 5th cycle (as shown in Figure 6b), as displayed in Table 3. It is interesting to note that the capacity in the 4 V region

of C-Cr is lower than that of C-1.5, although its higher Mn^{3+} content derived from the XPS results. This observation suggests that Cr-doping in LNMO spinel may result in rich Mn^{3+} content in the surface. After about five cycles, the CE of all of the samples increased up to 97.0%.

Table 3. Comparison of discharge capacities and Mn^{3+} contents in the LNMO-based samples.

sample	Discharge capacity (mAh g^{-1})		Amount of Mn^{3+} (%)
	5 V region	4 V region	
S-1.45	103.2	9.1	6.2
S-1.50	112.2	12.8	8.7
S-1.55	106.1	17.2	11.7
C-1.50	112.0	14.1	9.6
C-1.55	112.8	16.8	11.4
C-Cr	124.6	11.0	7.5

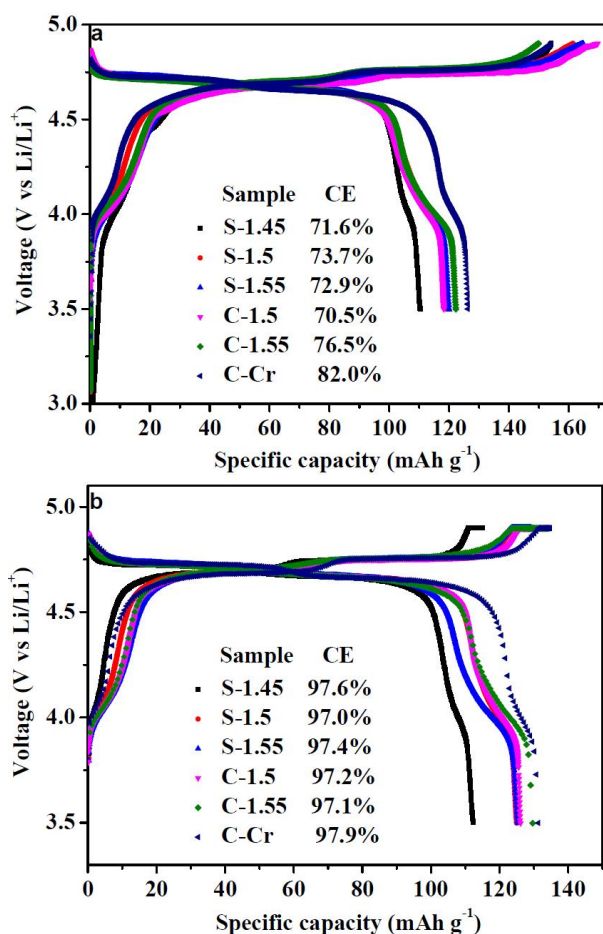


Figure 6. Charge/discharge curves and columbic efficiencies (CE) at the first and the fifth cycle of the six LNMO-based samples.

Figure 7 and Figure S5 show the rate performance and the voltage profiles of the various LNMO-based samples under various current densities in half-cell, respectively. The S-1.45 sample displays the lowest discharge capacity at any discharge current density in the six samples. Over 85% of their original discharge capacities could be still retained even at 10-C rate for all of the six samples, moreover, even after high rate testing, the discharge capacities could still return. In addition, the discharge voltage plateaus of the various LNMO-based samples under 10-C rate are higher than 4.5 V (Figure S5). This is attributed to the

intrinsically fast Li^{+} diffusion within the 3D spinel lattice.⁶ These observations suggest that the architecture of the porous LNMO-based samples are tolerant to various charge and discharge currents, a characteristic required for high power and high energy density applications. It is noted that both of S-1.5 and C-1.5 show quite similar discharge capacities at low rates (0.5 and 1.0 C), with differences less than 1.5 mAh g^{-1} . However, when the discharge current densities are higher than 2-C rate, the specific discharge capacity of the C-1.50 sample is much higher than that of the S-1.5 sample. This suggests that the cubic LNMO spinel displays superior rate performance. Similar phenomenon was observed in the S-1.55 sample. The superior rate performance of C-1.50 and S-1.55 samples may be attributed to the stronger peak of (111) facet in C-1.50 and higher Mn^{3+} content in the surface of S-1.55 than those of S-1.50, respectively. In addition, both of the C-1.55 and C-Cr samples exhibit higher specific capacities and better rate performance, comparing to other four samples. This may be ascribed to the synergetic effect of the cubic morphology and high surface Mn^{3+} content of these two samples, in which the cubic morphology of the LNMO-based spinels results in their high-active (111) crystal facet and the high surface Mn^{3+} content increases their conductivity. In fact, as seen in Figure 3b, the C-1.55 and C-Cr samples have similar relative peak intensity of (111) crystal plane, but Figure 7 clearly demonstrates much higher specific discharge capacity of C-Cr sample at high current densities (5 and 10 C-rates). This observation may be attributed to its larger cationic disorder, which will increase its lithium ion diffusion coefficient and decrease the small charge-transfer resistance.

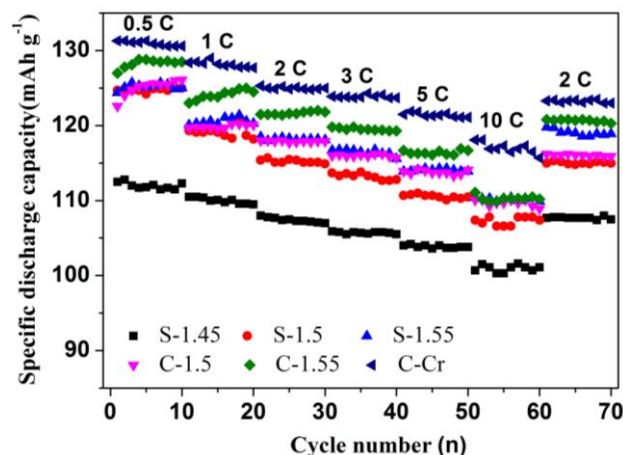


Figure 7. Rate performance of the six LNMO-based samples.

The cycling performance of the six as-prepared samples at 0.5 and 2-C rates were plotted in Figure 8. As indicated in Figure 8a, the six samples demonstrate good cycling performance at 25 °C at 0.5 C-rate with 81.3, 82.8, 83.5, 91.0, 92.8, and 91.1% of the highest capacity retained after 300 cycles for samples S-1.45, S-1.50, S-1.55, C-1.50, C-1.55, and C-Cr, respectively. When the samples were charged and discharged at 2 C-rate, similar cycle stability was observed. Specially, the specific discharge capacities are 109.3, 117.7, 120.4, 120, 122.4 and 127.8 mAh g^{-1} for S-1.45, S-1.50, S-1.55, C-1.50, C-1.55, and C-Cr, respectively, with the corresponding capacity retention (CR) ratios of 75.2, 85.3, 85.0, 90.0, 92.6, and 92.4% after 500 cycles. The CR capability

of the six samples is acceptable, however, the three cubic samples display much better cycle stability than that of the three spherical sample. This result may ascribed to the high exposure of high-active (111) crystal facet of the cubic samples.²⁶ Comparison of the cycle performance of the three cubic LNMO-based samples with different Ni/Mn ratio at different current densities (0.5 and 2 C-rates), no obvious difference was found, which may attributed to the similar (111) crystal plane intensity. In addition, the S-1.45 sample shows the worst cycle and rate performance at both 0.5 and 2-C rates, further demonstrating the high-active (111) crystal facet has very important effect on the cycle and rate performance of the LNMO-based material.

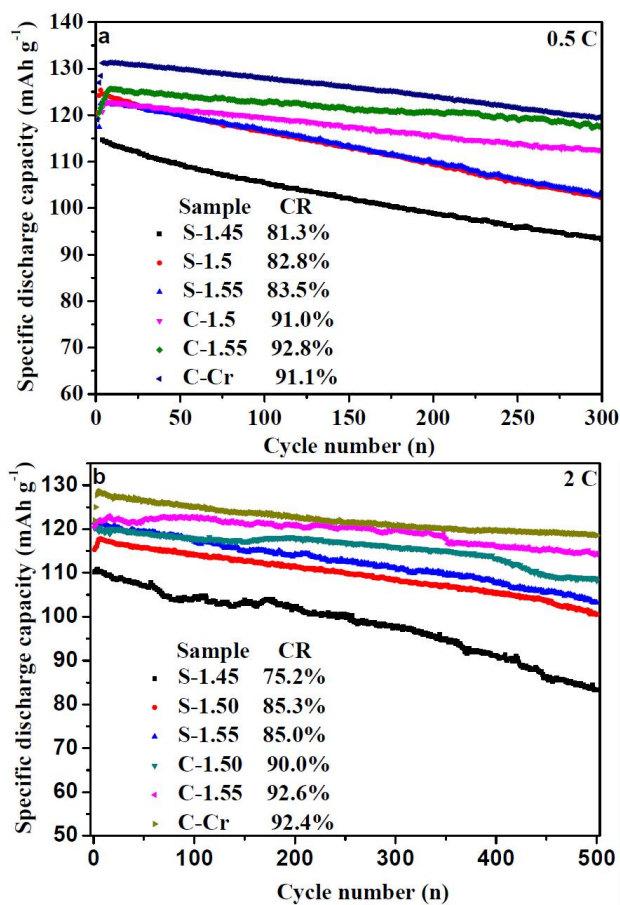


Figure 8. Comparison of the capacity retention (CR) of the six LNMO-based samples at different charge/discharge current densities.

Because both of the cubic C-1.55 and C-Cr samples display high specific discharge capacity at 0.5 and 2-c rate, we further investigate their cycle performance at high charge and discharge current density (5-C rate), and the corresponding results were displayed in Figure 9. Although these two samples show similar cycle performance at 0.5 and 2-C rates, remarkable differences in terms of capacity and capacity retention were observed when they cycled at 5-C rate. The C-Cr sample displays excellent cycle performance with CR ratio of 91.2% after 1000 cycles. The good cycle performance at high charge and discharge current density could be ascribed to the synergistic effect of its porous structure, high exposure of high-active (111) crystal plane, large cationic disorder and reasonable Mn^{3+} content in the crystal surface.

Generally, the capacity fade of LNMO is believed to originate from the instability of electrode and electrolyte under high voltage.^{14,18,56} The present Cr-doping sample has less surface Mn^{3+} content than that of the C-1.55 sample, which minimizes Mn disproportionative dissolution and Jahn-Teller structural distortion. On the other hand, the C-Cr sample has larger cationic disorder than that and C-1.55 sample, resulting in high rate performance due to low charge-transfer resistance and polarization loss.¹⁹ This is also demonstrated by the comparison of the discharge curves at different cycles of the C-Cr and C-1.55 samples (Figure S6). As shown in Fig. S7, the mean discharge voltage plateaus of the C-Cr sample is almost no decrease before 500 cycles and only drops from 4.61 in the 500th cycle to 4.57 V in the 1000th cycle, however, the mean discharge voltage of the C-1.55 sample drops from 4.62 in the 5th cycle to 4.55 V in the 1000th cycle.

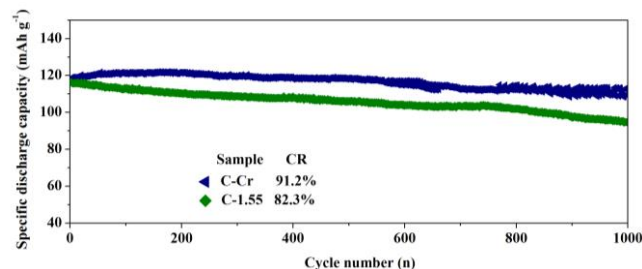


Figure 9. Comparison of the capacity retention (CR) of the C-1.55 and C-Cr samples at the charge and discharge current density of 5-C rate.

In order to gain a better understanding of the factors leading to the different rate performance of the C-Cr and C-1.55 samples, a series of voltammetry measurements were obtained and the corresponding results were shown in Figure 10 and Figure S7, respectively. As shown in Figure 10a, the CV curves of the C-Cr electrodes show two obvious redox peaks at ~ 4.7 V, even for the highest sweeping rate of 0.5 mV s^{-1} . The two redox peaks are also well consistent with the observed two-plateau charge and discharge profiles (Figure 6). In addition, the C-Cr electrode displays increasing peak current density (i_p) and widening separation potential within each redox couple as the potential scanning rate (ν) increases. Based on the previous results,²⁴ the peak current density (i_p) of the electrode for Li-ion diffusion can be estimated based on the following equation:

$$i_p = (2.69 \times 10^5) n^{3/2} A D_{Li}^{1/2} \nu^{1/2} C_{Li}^0$$

where n is the number of electrons per reaction species, A is the total surface area of the electrode (1.96 cm^2 in this case), D_{Li} is the diffusion coefficient in square centimeter per second, C_{Li}^0 is the bulk concentration in mole per cubic centimeter (which, in this case, is $0.02378 \text{ mol cm}^{-3}$),²⁴ and ν is the potential scan rate in volts per second. For a given charge number, the Li-ion diffusion coefficients can be calculated from the slope of peak current density versus the square root of the scan rate ($\nu^{1/2}$) (Fig. 10b). Detail experimental results are summarized in Table 4. The diffusion coefficients for the four different peaks are very similar, ranging from 7.72×10^{-11} to $2.01 \times 10^{-10} \text{ cm}^2/\text{s}$. These values are larger than the ones of C-1.55 (6.44×10^{-11} to $1.47 \times 10^{-10} \text{ cm}^2/\text{s}$) sample calculated for Li-ion diffusivity using CV data. The larger lithium ion diffusion coefficients imply that the porous C-Cr spinel favors faster lithium ion intercalation kinetics, resulting in its high rate performance.

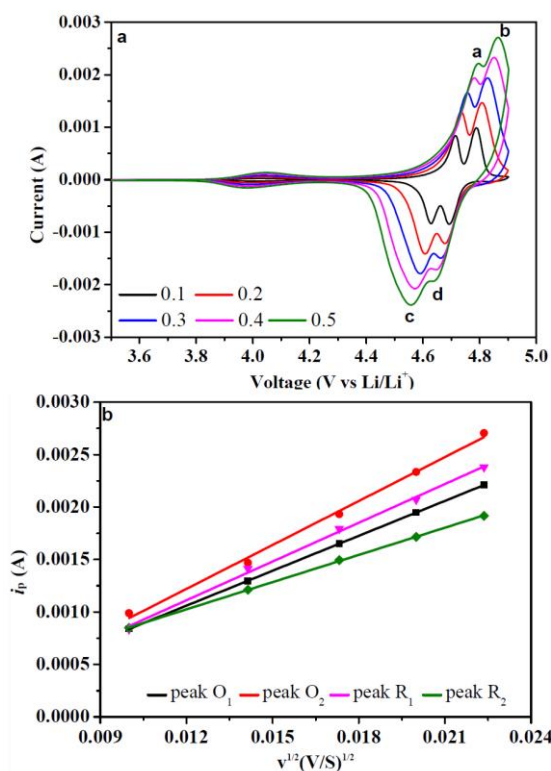


Figure 10. Cyclic voltammetry (CV) curves of the C-Cr electrode at scan rates from 0.1 to 0.5 mV s^{-1} . The oxidation (charging) peaks are labelled (a) and (b) while the reduction (discharging) peaks are labelled (c) and (d).

Table 4. Summary of the CV results obtained at different scanning rates and the Li^+ diffusion coefficients determined for the C-Cr electrode.^[a]

Scanning rate (mV/s)	Potential values/ V					
	EO_1	EO_2	ER_1	ER_2	ΔE_1	ΔE_2
0.1	4.713	4.792	4.628	4.691	0.085	0.101
0.2	4.734	4.808	4.607	4.678	0.127	0.130
0.3	4.758	4.826	4.592	4.662	0.166	0.164
0.4	4.782	4.850	4.572	4.654	0.210	0.205
0.5	4.795	4.863	4.558	4.646	0.237	0.217
D_{Li^+} ($10^{-11} \text{ cm}^2/\text{s}$)	5.90	6.00	4.33	6.35		

^[a] EO_1 : anodic peak potential, ER_1 : cathodic peak potential, ΔE : the separation between EO_1 and ER_1 . The subscript numbers 1 and 2 denote the redox couple at lower and higher potential, respectively.

EIS measurements are carried out to further understand the different electrochemical behaviors of the C-Cr and C-1.55 samples. Before cycling, both of the two samples only show one semicircle in the high- and medium-frequency regions and an inclined line in the low-frequency zone. Based on the fitting results, the C-Cr sample shows much smaller impedance than that of the C-1.55 sample (Figure 11a), which suggested the lower ohmic resistance for C-Cr sample. After the charge and discharge processes, both of the samples consist of a depressed semicircle in the high frequency, a semicircle in the medium frequency and a straight line in the low frequency (Figure 11b). The semicircle (R_{sei}) in the high frequency is ascribed to lithium ion diffusion through the solid electrolyte interface (SEI) after cycles, the semicircle in the high frequency can be usually assigned to the charge transfer impedance (R_{ct}), and the line is designated to a Warburg-type element reflecting the solid state diffusion of Li into the bulk of the active materials.^{9,30} when the electrodes were

cycled for 500 cycles, the R_{sei} (3.285 Ω) and R_{ct} (5.556 Ω) of the C-Cr sample are both lower than the R_{sei} (5.882 Ω) and R_{ct} (6.047 Ω) of the C-1.55 sample, respectively. This result may suggest that the C-Cr sample can alleviate electrolyte decomposition at high voltage and prevent the thick SEI film, which might be another reason for the better cyclability of the C-Cr sample compared to that of the C-1.55 sample.

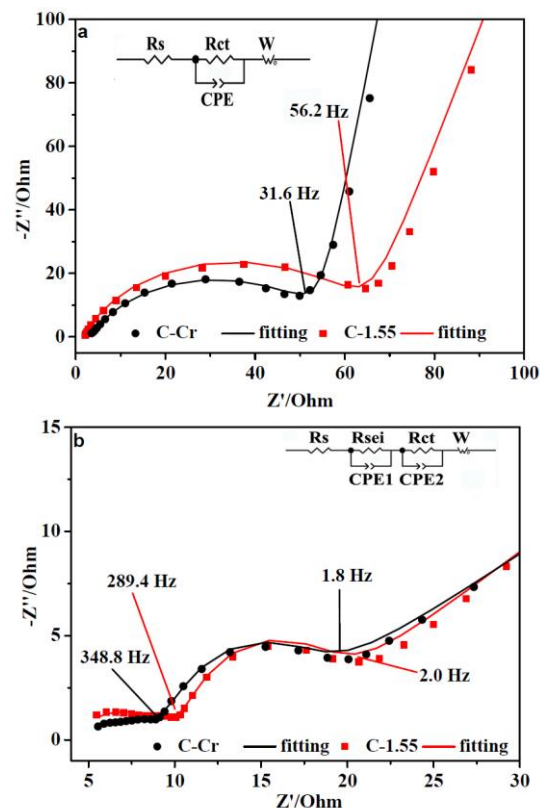


Figure 11. Comparison of impedance spectra (Nyquist plots) of the C-Cr and C-1.55 electrodes in the discharged state after different cycles at 5 C-rate, (a) the fresh cells and (b) the 500th cycle.

Conclusions

In conclusion, porous LNMO-based spinels with different morphologies and composition are prepared by a facile method via a self-supporting template and a eutectic molten lithium salt insertion reaction. The as-synthesized porous LNMO-based spinels exhibits different electrochemical performance because of their different morphology and composition, which results their different Mn^{3+} content in the crystal surface, phase purity, crystallographic planes structure as well as cationic disorder. Because of the absence of rock-salt phase, reasonable surface Mn^{3+} content, high exposure of the (111) crystal plane and high cationic disorder, the cubic Cr-doping LNMO spinel (C-Cr sample in this case) displays the highest specific capacity and the best rate and cycle performance among the six LNMO-based samples. It reaches ~ 132, 127 and 122 mAh g^{-1} at 0.5, 2 and 5 C-rates, respectively. The corresponding capacity retention ratio reaches 91.1%, 92.1% and 91.2% for up to 300, 500 and 1000 cycles at 0.5, 2 and 5-C rates, respectively. The high performances of porous Cr-doping LNMO microcubes make them become promising cathode materials for high performance

LIBs.

Acknowledgements

This work was supported by a linked project of China's Natural Science Foundation and Qinghai Province (Grant No. U1407124), Support from the Guangdong Province's Natural Science Foundation, the Guangzhou Scientific and Technological Planning Project (2014J4500002) and the Fok Ying Tung Foundation (NRC07/08.EG01).

Notes and references

¹⁰ ^a the Key Laboratory of Fuel Cell Technology of Guangdong province, School of Chemistry and Chemical Engineering, South China University of Technology, Guangzhou, 510640, China; chyfdeng@scut.edu.cn;

^b Centre for Green Products and Processing Technologies, Guangzhou HKUST Fok Ying Tung Research Institute, Guangzhou 511458, China;

¹⁵ ^c Department of Chemical and Biomolecular Engineering, The Hong Kong University of Science and Technology, Clear Water Bay, Kowloon, Hong Kong, China, kechengh@ust.hk.

† Electronic Supplementary Information (ESI) available: See DOI: 10.1039/b000000x/

- 20 1 G. J. Jeong, Y. U. Kim, Y. J. Kim and H. J. Sohn, *Energy Environ. Sci.*, 2011, **4**, 1986.
- 2 J. M. Tarascon, N. Recham, M. Armand, J. N. Chotard, P. Barpanda, W. Walker and L. Dupont, *Chem. Mater.*, 2010, **22**, 724.
- 3 (a) B. L. Ellis, K. T. Lee and L. F. Nazar, *Chem. Mater.*, 2010, **22**, 691, (b) X. P. Gao and H. X. Yang, *Energy Environ. Sci.*, 2010, **3**, 174, (c) F. M. Courtel, H. Duncan, Y. Abu-Lebdeh and I. J. Davidson, *J. Mater. Chem.*, 2011, **21**, 10206.
- 4 A. Manthiram, K. Chemelewski and E. Lee, *Energy Environ. Sci.*, 2014, **7**, 1339.
- 5 5 D. Liu, W. Zhu, J. Trottier, C. Gagnon, F. Barray, A. Guerfi, A. Mauger, H. Groult, C. M. Julien, J. B. Goodenough and K. Zaghib, *RSC Adv.*, 2014, **4**, 154.
- 6 J. H. Kim, A. Huq, M. Chi, N. P.W. Pieczonka, E. Lee, C. A. Bridges, M. M. Tessema, A. Manthiram, K. A. Persson and B. R. Powell, *Chem. Mater.*, 2014, **26**, 4377.
- 7 Y. Shin and A. Manthiram, *Chem. Mater.*, 2003, **15**, 2954.
- 8 S. H. Oh, S. H. Jeon, W. Cho, C. S. Kim and B. W. Cho, *J. Alloy Compound.*, 2008, **452**, 389.
- 9 J. Liu and A. Manthiram, *J. Phys. Chem. B*, 2009, **113**, 15073.
- 10 10 J. Hassoun, K. Lee, Y. K. Sun and B. Scrosati, *J. Am. Chem. Soc.*, 2011, **133**, 3139.
- 11 D. W. Shin and A. Manthiram, *Electrochem. Commun.*, 2011, **13**, 1213.
- 12 G. B. Zhong, Y. Y. Wang, Z. C. Zhang and C. H. Chen, *Electrochim. Acta*, 2011, **56**, 6554.
- 13 J. Song, D. W. Shin, Y. H. Lu, C. D. Amos, A. Manthiram and J. B. Goodenough, *Chem. Mater.*, 2012, **24**, 3101.
- 14 D. W. Shin, C. A. Bridges, A. Huq, M. P. Paranthaman and A. Manthiram, *Chem. Mater.*, 2012, **24**, 3720.
- 15 15 G. B. Zhong, Y. Y. Wang and C. H. Chen, *J. Power Sources*, 2012, **205**, 385.
- 16 O. Sha, Z. Y. Tang, S. L. Wang, W. Yuan, Z. Qiao, Q. Xu and L. Ma, *Electrochim. Acta*, 2012, **77**, 250.
- 17 J. Cabana, M. Casas-Cabanas, F. O. Omenya, N. A. Chernova, D. L. Zeng, M. S. Whittingham and C. P. Grey, *Chem. Mater.*, 2012, **24**, 2952.
- 18 J. Xiao, X. L. Chen, P. V. Sushko, M. L. Sushko, L. Kovarik, J. J. Feng, Z. Q. Deng, J. M. Zheng, G. L. Graff, Z. M. Nie, D. W. Choi, J. Liu, J. G. Zhang and M. S. Whittingham, *Adv. Mater.*, 2012, **24**, 2109.
- 19 19 D. W. Shin, G. A. Bridges, A. Huq, M. P. Paranthaman and A. Manthiram, *Chem. Mater.*, 2013, **25**, 768.
- 20 E. S. Lee and A. Manthiram, *J. Mater. Chem. A*, 2013, **1**, 3118.
- 21 Y. X. Qian, Y. F. Deng, L. N. Wan, X. S. Qin and G. H. Chen, *J. Phys. Chem. C*, 2014, **118**, 15581.
- 22 D. Liu, C. Gagnon, J. Trottier, A. Guerfi, D. Clément, P. Hovington, A. Mauger, C. M. Julien and K. Zaghib, *Electrochem. Commun.*, 2014, **41**, 64.
- 23 M. Kunduraci and G. G. Amatucci, *Electrochim. Acta*, 2008, **53**, 4193.
- 24 X. L. Zhang, F. Y. Cheng, K. Zhang, Y. L. Liang, S. Q. Yang, J. Liang and J. Chen, *RSC Adv.*, 2012, **2**, 5669.
- 25 Y. X. Qian, Y. F. Deng, Z. C. Shi, Y. B. Zhou, Q. C. Zhuang and G. H. Chen, *Electrochem. Commun.*, 2013, **27**, 92.
- 26 75 26 K. R. Chemelewski, D. W. Shin, W. Li and A. Manthiram, *Chem. Mater.*, 2013, **25**, 2890.
- 27 K. R. Chemelewski, D.W. Shin, W.Li and A. Manthiram, *J. Mater. Chem. A*, 2013, **1**, 3347.
- 28 S. F. Yang, J. Chen, Y. J. Liu and B. L. Yi, *J. Mater. Chem. A*, 2014, **2**, 9322.
- 29 80 29 K. R. Chemelewski, W. Li, A. Gutierrez and A. Manthiram, *J. Mater. Chem. A*, 2013, **1**, 15334.
- 30 B. Hai, A. K. Shukla, H. Duncan and G. Y. Chen, *J. Mater. Chem. A*, 2013, **1**, 759.
- 31 85 31 H. B. Lin, Y. M. Zhang, H. B. Rong, S. W. Mai, J. N. Hu, Y. H. Liao, L. D. Xing, M. Q. Xu, X. P. Li and W. S. Li, *J. Mater. Chem. A*, 2014, **2**, 11987.
- 32 M. Kunduraci, J. F. Al-Sharab and G. G. Amatucci, *Chem. Mater.*, 2006, **18**, 3585.
- 33 90 33 G. Q. Wang, J. Xie, C. Y. Wu, S. C. Zhang, G. S. Cao and X. B. Zhao, *J. Power Sources*, 2014, **265**, 118.
- 34 C. J. Jafta, M. K. Mathe, N. Manyala, W. D. Roos, K. I. Ozoemena, *ACS Appl. Mater. Interfaces*, 2013, **5**, 7592.
- 35 S. Brutti, G. Greco, P. Reale and S. Panero, *Electrochim. Acta*, 2013, **106**, 483.
- 36 95 36 N. M. Asl, J.H. Kim, N. P. W. Pieczonka, Z. Liu and Y. Kim, *Electrochem. Commun.*, 2013, **32**, 1.
- 37 J. H. Kim, N. P. W. Pieczonka, Z. Li, Y. Wu, S. Harris and B. R. Powell, *Electrochim. Acta*, 2013, **90**, 556.
- 38 100 38 A. Kraysberg and Y. Ein-Eli, *Adv. Energy Mater.*, 2012, **2**, 922.
- 39 K. M. Shaju, P. G. Bruce, *Dalton Trans.*, 2008, **37**, 5471.
- 40 J. G. Yang, X. P. Han, X. L. Zhang, F. Y. Cheng and J. Chen, *Nano Res.*, 2013, **6**, 679.
- 41 A. V. Potapenko, S. I. Chernukhina, I. V. Romanovab, K. Sh. Rabadanovc, M. M. Gafurovc and S. A. Kirillova, *Electrochim. Acta*, 2014, **134**, 442.
- 42 105 42 Y. Xue, Z. B.Wang, F. D.Yu, Y. Zhang and G. P Yin, *J. Mater. Chem. A*, 2014, **2**, 4185.
- 43 H. B. Lin, Y. M. Zhang, J. N. Hu, Y. T. Wang, L. D. Xing, M. Q. Xu, X. P. Li and W. S. Li, *J. Power Sources*, 2014, **257**, 37.
- 44 110 44 J. Wang, W. Q. Lin, B. H. Wu, J. B. Zhao, *J. Mater. Chem. A*, 2014, **2**, 16434.
- 45 Y. K. Sun, S. M. Oh, H. K. Park and B. Scrosati, *Adv. Mater.*, 2011, **23**, 5050.
- 46 115 46 L. Zhou, D. Y. Zhao and X. W. Lou, *Angew. Chem., Int. Ed.*, 2012, **51**, 239.
- 47 X. L. Zhang, F. Y. Cheng, J. G. Yang and J. Chen, *Nano Lett.*, 2013, **13**, 2822.
- 48 Y. F. Deng, Y. B. Zhou, Z. C. Shi, X. Zhou, X. Quan and G. H. Chen, *J. Mater. Chem. A*, 2013, **1**, 8170.
- 49 120 49 H. G. Zhu, E. W. Stein, Z. H. Lu, Y. R. M. Lvov and M. J. McShane, *Chem. Mater.*, 2005, **17**, 2323.
- 50 18 Z. R. Chang, Z. J. Chen, F. Wu, X. Z. Yuan and H. J. Wang, *Electrochim. Acta*, 2009, **54**, 6529.
- 51 125 51 J. S. Kim, K. Kim, W. Cho, W. H. Shin, R. Kanno and J. W. Choi, *Nano Lett.*, 2012, **12**, 6358.
- 52 W. Tang, Y.Y. Hou, F.X. Wang, L.L. Liu, Y.P. Wu and K. Zhu, *Nano Lett.*, 2013, **13**, 2036.
- 53 Amdouni, N.; Zaghib, K.; Gendron, F.; Mauger, A.; Julien, C. M. *Ionics*, 2006, **12**, 117.
- 54 130 54 C. V. Ramana, M. Massot and C. M. Julien, *Surf. Interface Anal.*, 2005, **37**, 412.
- 55 D. Liu, Y. Lu and J. B. Goodenough, *J. Electrochem. Soc.*, 2010, **157**, A1269.
- 56 135 56 J. B. Goodenough and K. S. Park, *J. Am. Chem. Soc.*, 2013, **135**, 1167.